Supporting Information for

Wetting state transition of individual condensed droplet on pillared textured surfaces

Chenlei Chu,[1,5] Yingang Zhao,[1] Pengfei Hao,[1,2] and Cunjing Lv[1,3,4*]

[1]Department of Engineering Mechanics, Tsinghua University, 100084 Beijing, China

[2]Tsinghua University(School of Materials Science and Engineering)-AVIC Aerodynamics Research Institute Joint Research Center for Advanced Materials and Anti-Icing, Tsinghua University, 100084 Beijing, China

[3]Center for Nano and Micro Mechanics, Tsinghua University, 100084 Beijing, China

[4]State Key Laboratory of Tribology in Advanced Equipment (SKLT), Tsinghua University, 100084 Beijing, China

[5]Beijing Institute of Spacecraft Environment Engineering, 100094 Beijing, China

Content

S1. Lattice Boltzmann Method (LBM) simulations

S2. Surface Evolver (SE) simulations

S3. Theoretical analyses

S4. Experimental procedure

Movie legend

References

---

* To whom correspondence should be addressed. Email: cunjinglv@tsinghua.edu.cn

S1. Lattice Boltzmann Method (LBM) simulations

S1.1. Introduction of the simulations by employing LBM

Lattice Boltzmann method (LBM) is developed based on the lattice gas automata.[1] The fundamental idea of LBM is to solve the discrete lattice Boltzmann equation on the regular lattices. LBM owns a lot of advantages, such as simple arithmetic calculations, more efficient of parallelism and feasible abilities of complex boundaries. In this regard, LBM is successfully applied in simulating the problems of flow in porous materials,[2] particle suspensions,[3] static and dynamic wetting phenomena on smooth and rough surfaces[4,5] and so on.

Here, the wetting behavior of droplet interacted with the pillars is simulated by employing a three-dimensional D3Q19 model with Bhatnagar-Gross-Krook approximation which is a simple linearized version of the collision operator that makes use of a single relaxation time towards the local equilibrium[6]. The lattice Boltzmann equation from a discrete kinetic equation for the particle distribution function is

$$f_i\left(\mathbf{r}+\mathbf{e}_i\Delta t, t+\Delta t\right)=f_i\left(\mathbf{r},t\right)-\frac{\left[f_i\left(\mathbf{r},t\right)-f_i^{\mathrm{eq}}\left(\mathbf{r},t\right)\right]}{\tau}, \tag{S1}$$

where f_i is the particle velocity distribution function along the i-th direction (i = 0, 1, 2, … 18), $\mathbf{r}$ is the position of the lattice, $\mathbf{e}_i$ is the local particle velocities, Δt is the time increment, and τ is the collision time. Moreover, the equilibrium distribution function $f_i^{\mathrm{eq}}(\mathbf{r}, t)$ is defined as

$$f_i^{\mathrm{eq}}\left(\mathbf{r},t\right)=w_i\rho\left(\mathbf{r}\right)\left[1+3\frac{\mathbf{e}_i\cdot\mathbf{u}}{c^2}+\frac{9}{2}\frac{\left(\mathbf{e}_i\cdot\mathbf{u}\right)^2}{c^4}-\frac{3}{2}\frac{\mathbf{u}^2}{c^2}\right], \tag{S2}$$

where the weight w_i are 1/3 for the rest particles (i = 0), 1/18 for i = 1 ~ 6 and 1/36 for i =7 ~ 18, respectively. c is the basic speed on the lattice. $\rho(\mathbf{r})$ and $\mathbf{u}$ respectively represent the fluid density and velocity, and they are defined as follows

$$\rho = \sum_{i=0}^{18} f_i, \qquad \mathbf{u} = \frac{\sum_{i=0}^{18} f_i \mathbf{e}_i}{\rho}. \tag{S3}$$

By incorporating nonlocal interactions among the fluid particles, we can simulate the interfacial energy. Regarding the approach developed by Shan and Chen,[7] we consider a fluid-fluid interaction as follows

$$\mathbf{F}_{\mathrm{G}}(\mathbf{r}) = -G\psi(\mathbf{r}) \sum_{i=0}^{18} w_i \psi(\mathbf{r} + \mathbf{e}_i) \mathbf{e}_i, \tag{S4}$$

where the weight w_i are 0 for $|\mathbf{e}_i| = 0$, 1/18 for $|\mathbf{e}_i| = 1$ and 1/36 for $|\mathbf{e}_i| = \sqrt{2}$, respectively. G represents the interaction strength, and we adopt $\psi(\mathbf{r}) = 1 - \exp[-\rho(\mathbf{r})]$ as the interaction potential. Moreover, we use the following interaction potential as the interaction between the fluid and solid phases

$$\mathbf{F}_{\mathrm{w}}(\mathbf{r}) = -G_{\mathrm{w}}\psi(\mathbf{r}) \sum_{i=0}^{18} w_i s(\mathbf{r} + \mathbf{e}_i) \mathbf{e}_i, \tag{S5}$$

where G_{w} represents the interaction strength between the fluid and solid. $s = 0$ and $s = 1$ are defined for the corresponding lattice points where they are in fluid and solid phases, respectively. The fluid-fluid interfacial energy and solid-fluid interfacial energy are adjusted by changing the fluid-fluid interaction strength G and the solid-fluid interaction strength G_{w}, respectively. By this way, we can simulate the contact angle ranging from 0° to 180°.

When we take consideration of the fluid-fluid interaction and the fluid-solid interaction, the local fluid velocity is determined as follows

$$\mathbf{u}'(\mathbf{r}) = \mathbf{u}(\mathbf{r}) + \frac{\tau}{\rho(\mathbf{r})} \left[\mathbf{F}_{\mathrm{G}}(\mathbf{r}) + \mathbf{F}_{\mathrm{w}}(\mathbf{r}) \right], \tag{S6}$$

where $\mathbf{u'(r)}$ is the updated fluid velocity of the next iteration.

S1.2. Description of the simulation systems

LBM has its own unit, i.e., size (lu), mass (mu) and time (ts). Since we do not consider the size effect, we use dimensionless formulas in the LBM simulations, and we mainly keep $S/L = 1.5$ as constant, with S and L being the spacing and width of the pillars, respectively (later we will discuss more values of S/L, and we will see that S/L does not change the main conclusion of the paper). Moreover, different contact angles are realized by varying the value of G_w. The box size in our simulations is 160 lu × 160 lu × 181 lu (length × width × height), and the width of the square pillar is $L = 6$ lu. The entire time step is typically on the order of 10^4 ts. Moreover, since it is difficult to introduce nanostructures on the surface of the micropillars, we assign specific values of the contact angle on the surfaces of the micropillars. Here, it is stressed that in real experiments, the nanostructures would vary the wetting behaviors of the condensed droplet, however, which is beyond the scope of the simulation capability.

In experiments, the droplet naturally grows up and its volume increases due to condensation. To simulate a uniform growth of the droplet, in our simulations, we set a source which is always at the mass center of the droplet, and the source has a spherical shape of radius 3 lu which is very small compared with the droplet. To suppress the dynamics, the source with outflow of a very small mass flow rate is employed to guarantee that the droplet quasi-statically increases. It is stressed that in this study, we mainly focus on the quasi-static process before the wetting state transition of the droplet, but not the dynamic process.

As shown in Fig. S1, two cases of simulations are exemplarily given to show the influences of the pillar height H on the wetting state transitions. In these examples, $\theta = 140°$ and $S/L = 1.5$, whereas $H/L = 5.5$ and $H/L = 2.5$ in Figs. S1(a) and S1(b), respectively. When the pillars are higher (i.e., $H/L = 5.5$), the droplet dewets spontaneously from the pillars when $h_d < H$, where h_d is defined as the vertical position of its maximum transverse cross-section (with the width

d_{max}). We call this case the Cassie-jumping mode. However, when the pillars are lower (i.e., $H/L = 2.5$), the droplet grows until $h_d \geq H$, and then it dewets from the pillars, and we call this case the Cassie-detaching mode. These results suggest that the spontaneous dewetting of droplet is more likely to happen on the substrate with higher pillars.
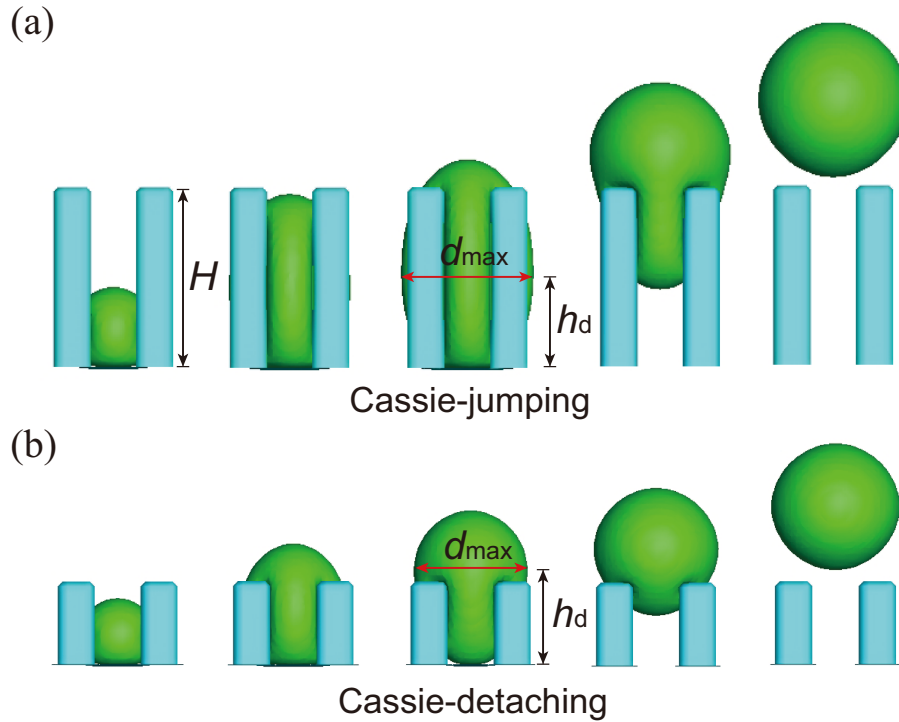
(a)

Cassie-jumping

(b)

Cassie-detaching

Fig. S1. LBM simulation results. (a) Cassie-jumping transition mode with $\theta = 140°$, $S/L = 1.5$ and $H/L = 2.5$. (b) Cassie-detaching transition mode with $\theta = 140°$, $S/L = 1.5$ and $H/L = 5.5$. d_{max} represents the maximum width of the transverse cross-section, and h_d represents the corresponding vertical height of that cross-section.

S2. Surface Evolver simulations

The confined droplets in our study have very complex geometry. Due to the absence of analytical solution, one public domain software package called Surface Evolver (SE),[8] developed by K. Brakke, is used to simulate the morphology of droplets confined in the pillars. The basic concept of SE is to minimize the energy and find the equilibrium shape of interfaces subject to the user defined surface tensions, interface areas, and constraints. SE can handle an arbitrary topology of the liquid surface, and during the calculations, it can report total energies, surface areas of the interface, and many other variable quantities.[9,10]

In the simulation, the total surface energy E is defined as $E = \gamma(A_{LV} - A_{SL} \cos\theta)$, in which A_{LV} and A_{SL} are the areas of the liquid-vapor and the solid-liquid interfaces, respectively. θ is the contact angle defined based on the Young's equation $\cos\theta = (\gamma_{SV} - \gamma_{SL})/\gamma$, in which γ, γ_{SL} and γ_{SV} are the liquid-vapor, solid-liquid and solid-vapor interfacial tensions, respectively. Concerning in SE simulations, it is not very convenient to add two-tier structures, we assign specific contact angles on the surfaces of the micropillar, which is similar to the aforementioned LBM simulations.
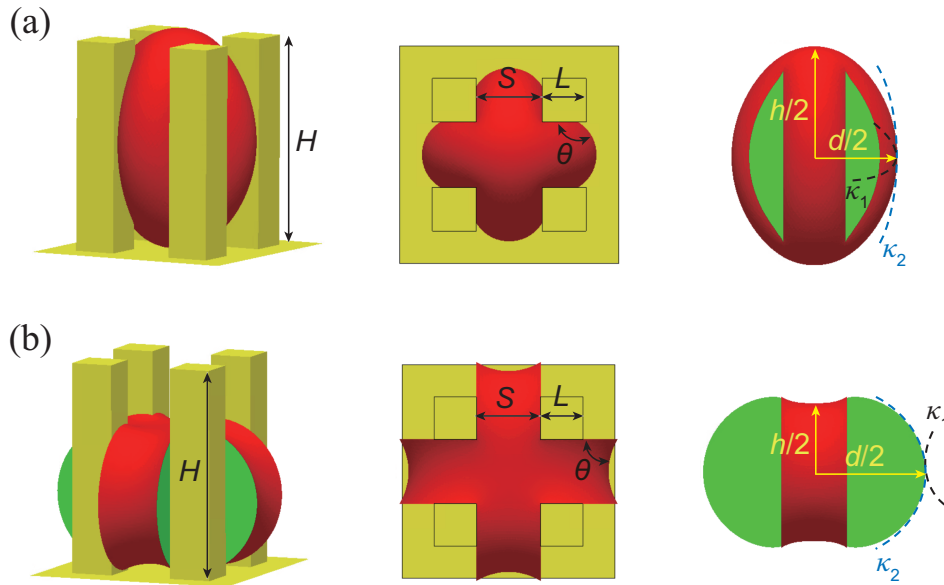

Fig. S2. SE simulation results showing the geometry of droplets confined in the micropillars. The red and green colors represent the liquid-vapor and the solid-liquid areas, respectively. H, S, L denote the height, spacing and width of the pillar. θ is the contact angle between water and the surface of the pillar. κ_1 and κ_2 are the two main curvatures. d and h are the width and height of the droplet, respectively. Two examples of the equilibrium wetting state with $\theta = 150°$ (a) and $\theta = 60°$ (b) are given.

As shown in Fig. S2(a), we give the equilibrium wetting state of a superhydrophobic droplet ($\theta = 150°$) confined in four neighboring pillars. Here, $S/L = 1.5$ and $H/L = 5.5$. The yellow, green and red colors represent the solid-vapor, solid-liquid and liquid-vapor interfaces, respectively. Fig. S2(b) shows the equilibrium wetting state of a hydrophilic droplet ($\theta = 60°$). The spacing and height of the pillars in Fig. S2(a) respectively have the same values as them in Fig. S2(b).

Here, we emphasize that in order to make the solid-liquid (green color) interface more visible in Fig. S2(b) and make comparisons with Fig. S2(a), the appearance of the pillars in Fig. S2(b) is just displayed the same as Fig. S2(a). In Fig. S2(b), the value of L is much larger, otherwise the droplet cannot be confined. However, for certain values of the contact angle and the volume of the droplet, when the values of S and H are given, and meanwhile the value of L is large enough, the configuration of the droplet in the equilibrium wetting state will not depend on L. This is the reason that in Fig. S2(b), the width of the pillars is not fully displayed.

For convenience, we use dimensionless parameters. We choose the pillar length L as the length scale factor, together with the surface tension γ, all the geometrical and physical parameters are normalized as

$$\bar{S} = \frac{S}{L}, \quad \bar{H} = \frac{H}{L}, \quad \bar{h} = \frac{h}{L}, \quad \bar{A} = \frac{A}{L^2}, \quad \bar{\kappa} = \kappa L, \quad \Delta\bar{P} = \frac{\Delta P}{\gamma/L}, \quad E = \frac{E}{\gamma L^2}, \quad (S7)$$

where S, H, h, A, κ, ΔP and E denote spacing and height of the pillar, height, area, curvature, pressure and energy of the droplet, respectively.

S3. Theoretical analyses
S3.1. Laplace pressure
In the following, we will give a general formula to relate the Laplace pressure ΔP to the relevant geometrical parameters. Considering that in real case the condensed droplet is sufficiently small, the effect of gravity is negligible in the present study. Moreover, it is emphasized that in this section, we investigate the situation before the occurrence of the wetting state transition. Thus, the droplet is in an equilibrium state with a uniform pressure throughout the droplet. Based on the differential geometry,[11] there are two main curvatures κ_1 and κ_2 at any point of the liquid-vapor interface, and the total curvature $2\kappa = \kappa_1 + \kappa_2$ is constant.[12] In our case, the droplet is like a cross intersection of two sandwich droplets, and there is no analytical solution to either describe its morphology or ΔP. We first choose the point at the equator of the droplet to make

analyses. κ_1 could be linked to S, and we could obtain an approximation $\kappa_1 \approx -2\cos\theta/S$. On the other hand, the cross-section of the droplet in the vertical direction is like an ellipse,[13] even though we could not directly obtain the exact value of κ_2, it is reasonable to express it as the function of θ and $1/h$, i.e., $\kappa_2 \approx f(\theta, 1/h)$, and we are able to approach it by Taylor series. Thus, for arbitrary contact angles, we assume that the relationship between 2κ and h has the following dimensionless formula

$$\Delta\bar{P} = 2\bar{\kappa} = -\frac{2\cos\theta}{\bar{S}} + \alpha_1\left(\frac{1}{\bar{h}}\right) + \alpha_2\left(\frac{1}{\bar{h}}\right)^2 + \alpha_3\left(\frac{1}{\bar{h}}\right)^3 + \cdots, \tag{S8}$$

where α_1, α_2 and α_3 are coefficients and they are the functions of the contact angle θ. In this regard, we obtain

$$\frac{\partial(2\bar{\kappa})}{\partial\left(\frac{1}{\bar{h}}\right)} = \alpha_1 + 2\alpha_2\left(\frac{1}{\bar{h}}\right) + 3\alpha_3\left(\frac{1}{\bar{h}}\right)^2 + \cdots. \tag{S9}$$

As shown in Fig. S3, we give the dimensionless result of $\partial(2\kappa)/\partial(1/h)$ vs. $1/h$, in other words, $\partial(\Delta P)/\partial(1/h)$ vs. $1/h$, in the dimensionless form.
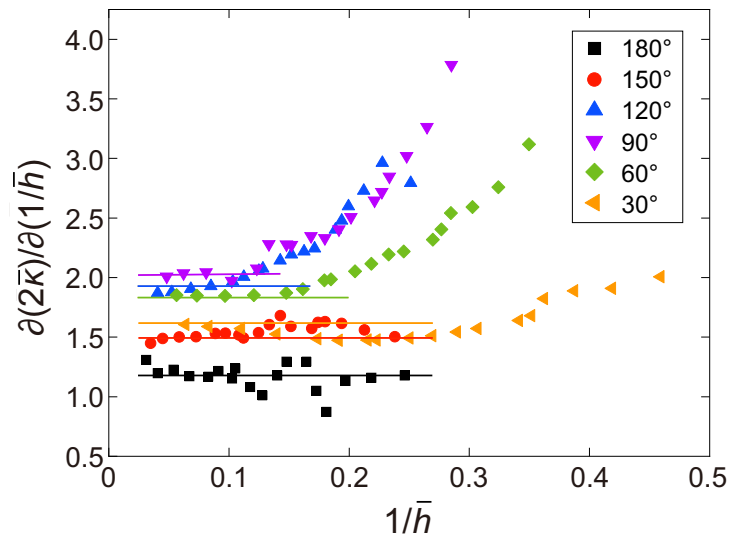

Fig. S3. Relationship between $\partial(2\kappa)/\partial(1/h)$ and $1/h$ in the dimensionless form. The dots are SE simulation

results, and the solid lines with corresponding colors indicate the values of α_1 when $1/h \rightarrow 0$.

As we know, $\alpha_1 = \partial(2\bar{\kappa})/\partial(1/\bar{h})$ when $1/\bar{h} = 0$. As shown in Fig. S3, we find that $\partial(2\bar{\kappa})/\partial(1/\bar{h})$ indeed approaches a constant for a specific θ when $1/\bar{h} = 0$ (solid line), and $\alpha_1 \approx 1.17, 1.55, 1.88, 2.00, 1.85$ and 1.60 are extracted for $\theta = 180°, 150°, 120°, 90°, 60°$ and $30°$, respectively. Then, we plot α_1 as a function of θ in Fig. S4.
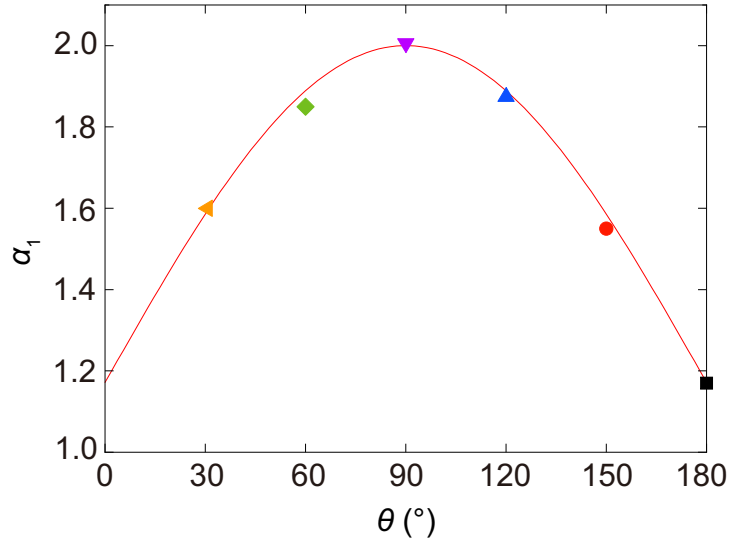

Fig. S4. Relationship between α_1 and θ ranging from 0° to 180°. The dots are the results obtained from Fig. S3 (solid lines), and the red curve is the result of eqn (S12).

We notice that $\alpha_1|_{\theta=180°} \approx 1.17 \approx 4 - 2\sqrt{2}$ and $\alpha_1|_{\theta=90°} \approx 2.0$. To find α_1, we build an approximate relationship

$$\alpha_1 = 4 - 2\sqrt{2} + g(\theta) \cdot \frac{2 - (4 - 2\sqrt{2})}{2 - 0} = 4 - 2\sqrt{2} + g(\theta)(\sqrt{2} - 1), \tag{S10}$$

where eqn (S10) must satisfy $g|_{\theta = 180°} = 0$ and $g|_{\theta = 90°} = 2$. We further approximate

$$g(\theta) \approx 2\sin\theta. \tag{S11}$$

Next, substituting eqn (S11) into eqn (S10), we get the following approximate solution

$$\alpha_1 = 4 - 2\sqrt{2} + 2\left(\sqrt{2} - 1\right)\sin\theta = 2\left(\sqrt{2} - 1\right)\left(\sqrt{2} + \sin\theta\right). \tag{S12}$$

As we can see from Fig. S4, the theoretical result obtained from eqn (S12) (red curve) is very well consistent with SE simulation results (dots). Finally, a combination of eqn (S8), Eq. (S12) and Young-Laplace equation $\Delta P = 2\kappa\gamma$ leads to eqn (1) in the main paper.
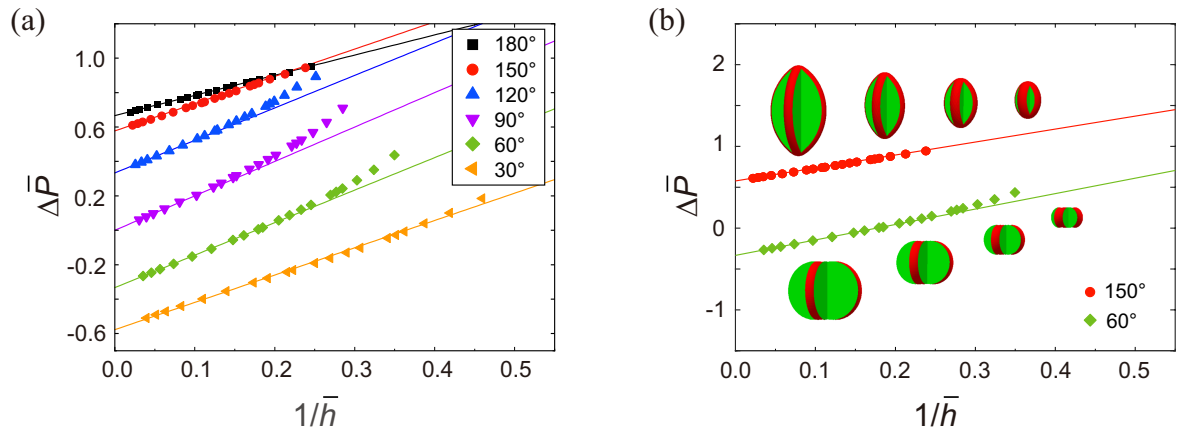

Fig. S5. (a) Relationship between ΔP and $1/h$ in dimensionless form. The dots are simulation results obtained by SE, and the curves are theoretical results of eqn (1) in the main paper. (b) Two examples ($\theta = 150°$ and $\theta = 60°$) showing the evolutions of the droplet morphology.

Furthermore, in order to verify the generality of eqn (1), as shown in Fig. S6, we carry out more simulations with various values of S/L. The dots in Fig. S6(a) and Fig. S6(b) are simulation results of SE with $S/L = 1$ and $S/L = 3$, respectively, and the curves with the corresponding colors are the theoretical results obtained using eqn (1). It can be seen that the simulation results are in very good agreement with the theoretical results. In this regard, we conclude that eqn (1) in the main text is general even though in the above we build the theory by employing a specific value of S/L.
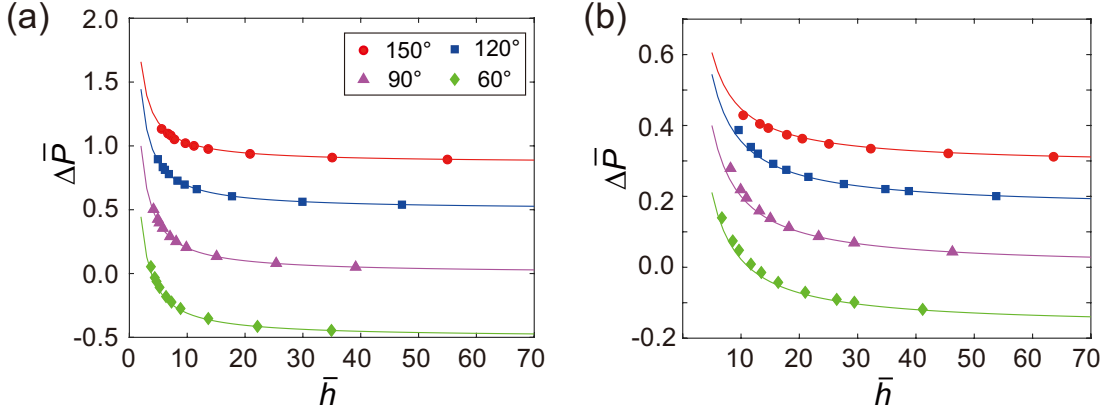
Fig. S6. Relationship between ΔP and h in dimensionless form. The dots are simulation results obtained by Surface Evolver (SE), and the curves with the corresponding colors are theoretical results of eqn (1) in the main text for different values of the contact angle. (a) $S/L = 1$; (b) $S/L = 3$.

S3.2. Some basic geometrical relationships

To find the criterion for the wetting state transition, we devote to finding some basic geometrical relationships. For the hydrophobic case, first, we will find the relationship between the width d and the height h of the droplet. Based on the results obtained by SE simulations, as shown in Fig. 3(b) of the main paper, we notice that the droplet height h has a linear relationship with the droplet width d.

One can imagine that, when the droplet grows and just touches the four pillars around it, it is an undeformed sphere having $h = d = \sqrt{2}S$. For a specific case when $\theta = 90°$ as shown in Fig. S7, the direction of the binormal of the liquid-vapor interface at any point of the solid-liquid-vapor three-phase contact line is always orthogonal to the surface of the pillar. During the growth, the droplet is close to a sphere, therefore, we approximate $d - \sqrt{2}S = h - \sqrt{2}S$. However, when $\theta \neq 90°$, the droplet deviates from a sphere, therefore, we approximate the relationship between d and h as $d - \sqrt{2}S = k(h - \sqrt{2}S)$, where k is a fitting coefficient which depends on the value of θ. Based on a best fit to the SE simulation results in Fig. 3(b) of the main paper, we obtain $k \approx 1 + (\cos\theta)/2$, and we have

$$d - \sqrt{2}S = \left(1 + \frac{\cos\theta}{2}\right)\left(h - \sqrt{2}S\right). \tag{S13}$$

We further write eqn (S13) into

$$d = \left(1 + \frac{\cos\theta}{2}\right)h - \frac{1}{\sqrt{2}}S\cos\theta. \tag{S14}$$

As shown in Fig. 3(b) of the main paper, eqn (S14) agrees with the simulation results very well.
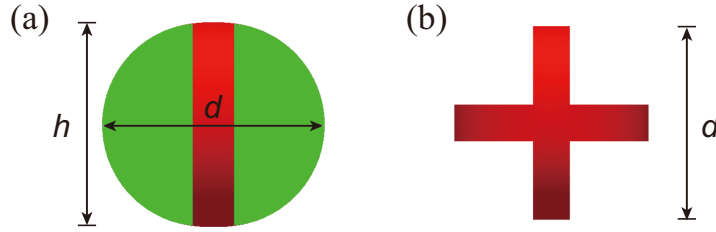

Fig. S7. Morphologies of a droplet from side (a) and top (b) views with the contact angle $\theta = 90°$. h and d represent the height and the width of the droplet along the vertical and the horizontal directions, respectively. The red and green colors represent the liquid-vapor and solid-liquid interfaces, respectively.

S3.3. Derivation of the critical condition for the Cassie-jumping mode

As shown in Fig. S8(a), we give the side view of a droplet when it reaches the critical condition for the Cassie-jumping mode. In other words, when the volume of the liquid further increases, the drop will jump out of the pillars, and this critical condition is the boundary between the Cassie-jumping and Cassie-detaching wetting state transition modes. In this case, the width and the height of the drop d and h reach their critical values d_c and h_c, respectively.

First, we will find the width w of the droplet in the transverse cross-section where its height is equal to the height of the pillars (Fig. S8(a)). Here, since the gravity is ignored and the droplet is tightly confined, we assume the profile (Fig. S8(b)) of the droplet confined between two neighboring pillars is circular (from the top view) with a radius R. Based on the geometrical

relationships $2R\sin(\theta - \pi/2) = S$ and $2R[1 - \cos(\theta - \pi/2)] + S = w$, we obtain
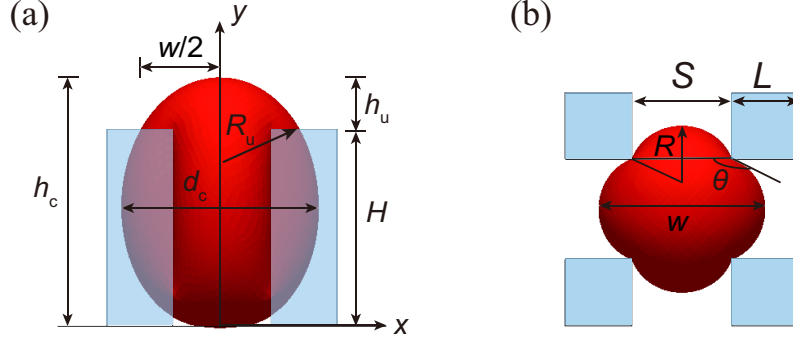
$$w = (1 - \sec\theta + \tan\theta)S.$$ (S15)

Fig. S8. Morphology of the droplet at the critical condition for the Cassie-jumping mode. The contact angle is $\theta = 160°$. (a) Morphology of the droplet from the side view. H is the height of the pillars, h_c and d_c are the critical height and the width of the droplet, h_u and R_u are the height and curvature radius (from the side view) of the droplet above the pillars. (b) Morphology of the droplet from the top view. w and R are the width and the curvature radius of the transverse cross-section which height is equal to the height of the pillars.

Next, we approximate the profile of the droplet as elliptical as shown from the side view in Fig. S8(a),[14] and we construct a two-dimensional Cartesian coordinate system. Then, we have

$$\frac{x^2}{\left(d_c/2\right)^2} + \frac{\left(y - h_c/2\right)^2}{\left(h_c/2\right)^2} = 1.$$ (S16)

Since the point $(w/2, H)$ is at the ellipse, we have

$$\frac{\left(w/2\right)^2}{\left(d_c/2\right)^2} + \frac{\left(H - h_c/2\right)^2}{\left(h_c/2\right)^2} = 1.$$ (S17)

As a consequence, eqn (S17) leads to

$$H = \frac{h_c}{2}\left[1 + \left(1 - \frac{w^2}{d_c^2}\right)^{\frac{1}{2}}\right]. \tag{S18}$$

Putting eqn (S14) and (S15) into eqn (S18), we have

$$H = \frac{h_c}{2}\left(1 + \sqrt{1 - \frac{4(1 - \sec\theta + \tan\theta)^2 S^2}{[(2 + \cos\theta)h_c - \sqrt{2}S\cos\theta]^2}}\right). \tag{2}$$

As shown in Fig. S9, the theoretical results of eqn (2) (red curve) are consistent very well with the simulation results of SE (black squares).
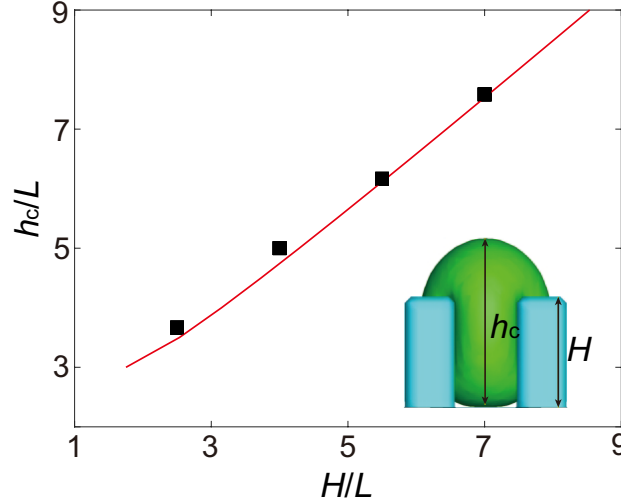

Fig. S9. Relationship between the critical height h_c of the droplet and the height H of the pillars in the dimensionless form. The black dots and the red curves represent the simulation results and the results of eqn (2), respectively. The contact angle is $\theta = 160°$.

Furthermore, as we know, the spontaneous jumping of the droplet is driven by a Laplace pressure difference at the bottom side ΔP_b and the upper side ΔP_u of the droplet.[15,16] Based on the morphology of the droplet shown in Fig. S8(a), we approximate the upper side as spherical with a radius R_u. Considering $R_u^2 = (R_u - h_u)^2 + (w/2)^2$, we have

$$\Delta P_{\mathrm{u}} = \frac{2\gamma}{R_{\mathrm{u}}} = \frac{16h_{\mathrm{u}}\gamma}{w^2 + 4h_{\mathrm{u}}^2}. \tag{S19}$$

Substituting eqn (S15) and $h_{\mathrm{u}} = h_{\mathrm{c}} - H$ into eqn (S19), we obtain eqn (3) in the main paper

$$\Delta P_{\mathrm{u}} = \frac{16(h_{\mathrm{c}} - H)\gamma}{(1 - \sec\theta + \tan\theta)^2 S^2 + 4(h_{\mathrm{c}} - H)^2}. \tag{3}$$

S3.4. Derivation of the critical condition for the Cassie-detaching mode

Considering the Cassie-detaching wetting state transition, we will calculate the Laplace pressure differences on the bottom side ΔP_{b} and the upper side ΔP_{u} of the droplet, and then find the critical condition. In other words, this critical condition is the boundary between the Cassie-detaching and Wenzel-collapsing wetting state transition modes. Based on the simulations and the geometries as shown in Fig. 4(b)(i) in the main paper from a three-dimensional point of view, when the droplet grows big enough and the width of its cap d beyond the top of the pillars is larger than the distance along the diagonal direction of the four pillars, i.e., $d > \sqrt{2}(S + 2L)$, the droplet cap will no longer sit on the pillars but gradually swallows the pillars. When the cap completely submerges the pillars, a Wenzel-collapsing wetting state translation will occur. Fig. 4(b)(iii) shows the critical state of the Wenzel-collapsing mode of the droplet. Since the droplet is sufficiently big compared with the height of the pillars, we approximate $R' \approx b + H$, where b is determined by $b = \sqrt{2}(S + 2L)\tan(\theta - \pi/2)/2$. The Laplace pressure of the top of the droplet $\Delta P_{\mathrm{u}} = 2\gamma/R' = 2\gamma/(b + H)$ could be obtained as

$$\Delta P_{\mathrm{u}} = \frac{4\gamma}{\sqrt{2}(S + 2L)\tan\left(\theta - \dfrac{\pi}{2}\right) + 2H}. \tag{5}$$

In this case, the Laplace pressure of the bottom side of the droplet approximately equals to $\Delta P_{\mathrm{b}} = -2\gamma\cos\theta/S$. In order to verify this conclusion, as shown in Fig. S10, we give the time evolution

of the morphology of a condensed droplet from different views. Figure S10(a) shows the side view of the droplet, in which the droplet keeps growing. As time progress, the spherical part of the liquid-vapor interface keeps, and later it swallows the pillars. Figure S10(b) shows the zoomed-in views of the central cross-section of the droplet (from the side view) closed to the bottom part. It can be seen that during growing, on the one hand, the part of the droplet trapped among the pillars is almost unchanged, on the other hand, the liquid-vapor meniscuses trapped among the pillar but which are above the bottom part are almost along the vertical direction, which means its meridional curvature approximately equals to zero, i.e., $\kappa_2 \approx 0$. Figure S10 (c) shows the time evolution of the cross-section of the droplet at $H/2$. It can be seen that the azimuthal curvature of the liquid-vapor meniscus remains unchanged during the growth of the droplet and is only related to the structural parameters and the wettability, i.e., $\kappa_1 = -2\gamma\cos\theta/S$. Therefore, we believe that in the process of droplet growth and collapse, the Laplace pressure at the bottom of the droplet (ΔP_b) remains unchanged, which could be approximately expressed as eqn (4), i.e., $\Delta P_b = (\kappa_1 + \kappa_2)\gamma = -2\gamma\cos\theta/S$.
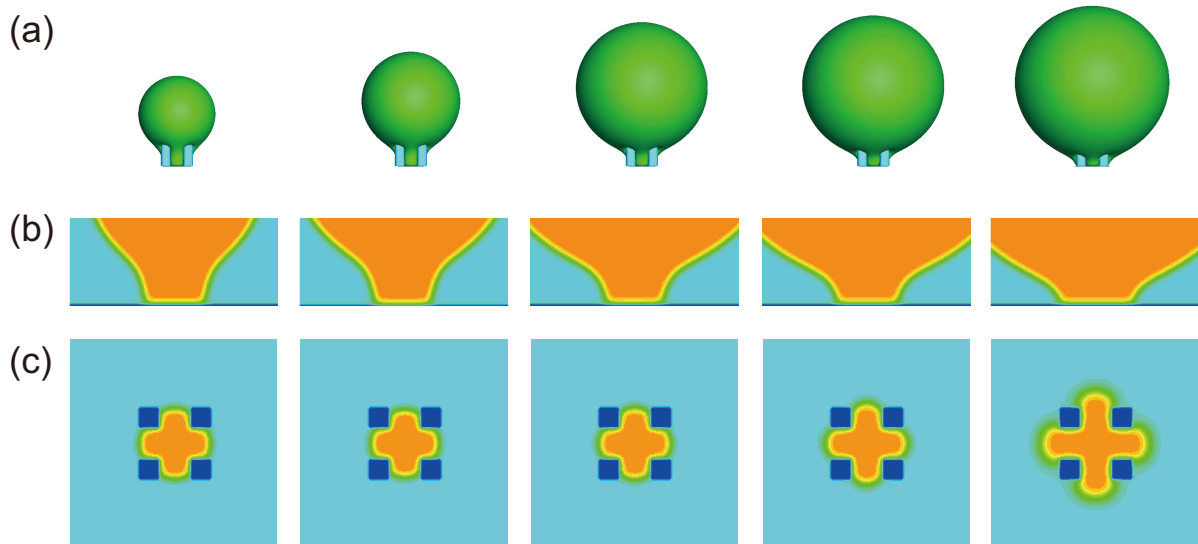

Fig. S10. Time evolution of a condensed droplet in the Wenzel-collapsing mode with $\theta = 100°$ and $H/L = 2.5$. (a) Side view of the droplet during the processes of growing up and collapsing; (b) Zoomed-in views of the central cross-section of the droplet (from the side view) closed to the bottom part, where the orange and the blue colors represent the liquid and gas phases, respectively; (c) Cross-section of the droplet at the height of $H/2$, where the dark blue color represents the cross-section of the pillars.

Therefore, the pressure difference $\delta P = \Delta P_b - \Delta P_u$ between the bottom and upper sides of the droplet can be obtained.

S4. Experimental procedure

S4.1. Sample fabrication and coating

Standard photolithography and deep reactive ion etching are used to create silicon micropillar arrays. To make the sample superhydrophobic, we employ a commercial superhydrophobic coating (Glaco Mirror Coat "Zero", Soft 99, Japan) consisting of hydrophobic nanoparticles dispersed in isopropanol. The samples are first sunk in the solvent, and then they are taken out and dried in air for 1 min. After that, the samples are put into an oven at 120 °C for 15 min.

These sinking and heating processes are repeated three times. After the above treatment, the contact angle of the flat silicon wafer reaches $\theta^* = 162 \pm 2°$. To obtain moderate hydrophobicity, the samples are treated with another commercial polyacrylate hydrophobic coating (Water Repellent Spray (3rd Generation, YACAIJIE, China) that mainly includes ployacrylates and propylene. After sinking a flat silicon wafer in the solvent, removing and drying for 10 min and repeating twice, the contact angle is $\theta^* = 123 \pm 2°$. Moreover, by employing molecular vapor deposition (MVD) to deposit FDTS ($C_{10}H_4C_{l3}F_{17}Si$) onto the sample, we could also obtain hydrophobicity. For a flat silicon wafer, after the treatment, the contact angle becomes $\theta^* = 109 \pm 3°$.

S4.2. Characterization of the surfaces

The micropillared surfaces are characterized by a field-emission scanning electron microscope (SEM) (Quanta FEG450). More details of the corresponding dimensions of the samples are given in Supporting Information Table 1.

As shown in Supporting Information Table S1, the width L and spacing S of the micropillars are equal, and the width of the micropillars ranges from 2 μm to 10 μm. There are two different heights H of the pillars, i.e., 6 μm and 8 μm. After making normalization by L, the micropillared

substrates have six different dimensionless heights. Moreover, as shown in Fig. S11, we give the topology of the corresponding pillars characterized by the SEM.

Table S1. Details of the geometric parameters of the micropillared samples employed in the experiments.

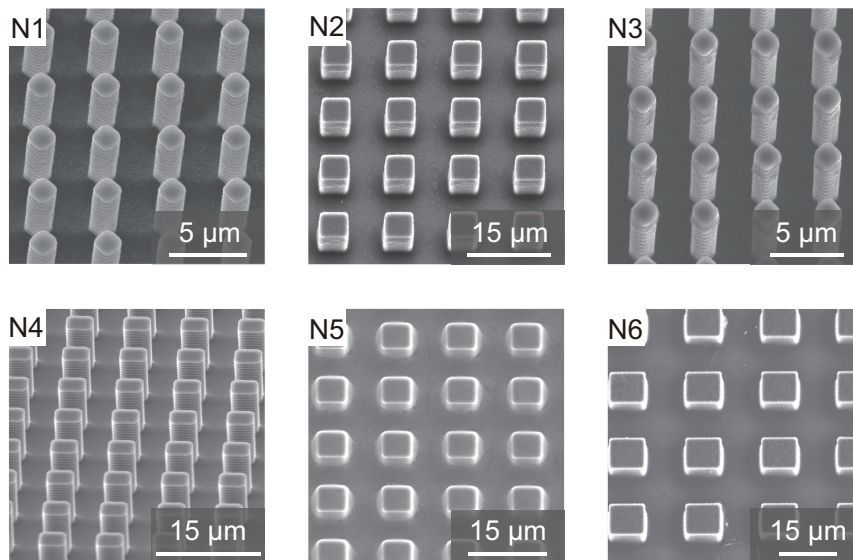| No.	L (μm)	S (μm)	H (μm)	S/L	H/L
1	2	2	6	1	3
2	6	6	6	1	1
3	2	2	8	1	4
4	4	4	8	1	2
5	6	6	8	1	1.33
6	10	10	8	1	0.8

Fig. S11. SEM images of the micropillared substrates. The sample numbers in Table S1 are marked as N1-N6, respectively, among which N1-N4 are bare pillars and N5-N6 are pillars coated with the commercial coating agent (Glaco, Soft99).[17,18]

S4.3. Contact angle measurement

Measurements of the contact angle and the contact angle hysteresis are performed at room temperature (about 25 °C) and a relative humidity of 40 %. An automatic microscopic contact angle meter (DSA25S, KRUSS, Germany) is employed. Before the measurement, all samples are cleaned by acetone, followed by deionized water, and finally dried by blowing nitrogen. To measure the contact angle, small droplets of 5 μl are smoothly deposited on the samples. By injecting and pumping back water from the droplet, the advancing and receding contact angles

θ_a and θ_r are measured, respectively (see Supporting Information Fig. S12).

In order to quantify the wettability of the substrates, we measure the apparent contact angle θ^*, the advancing contact angle θ_a and the receding contact angel θ_r of flat silicon wafers treated by different coatings. The detailed results are given in Table S2 and Fig. S12.

Table S2. Details of the apparent contact angle θ^*, the advancing contact angle θ_a and the receding contact angle θ_r of flat silicon wafers treated by different coatings.

No.	$\theta^*(°)$	$\theta_a(°)$	$\theta_r(°)$	Coating
1	162±2	167±2	156±3	Glaco
2	123±2	129±2	118±3	Polyacrylate
3	109±3	116±3	97±3	FDTS

(a) (b) (c)

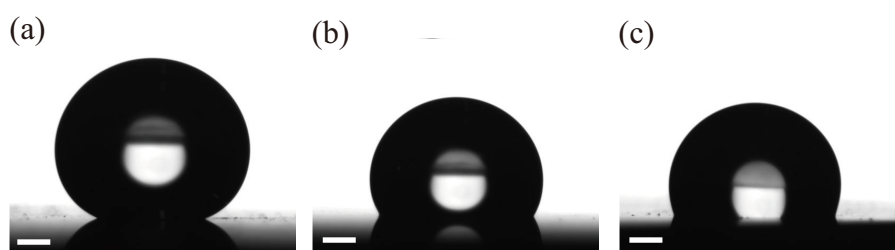**Fig. S12.** Contact angle measurements on flat silicon wafers coated with hydrophobic essences. (a) Glaco, $\theta^* = 162 \pm 2°$. (b) Fluoroacrylate, $\theta^* = 123 \pm 2°$. (c) FDTS, $\theta^* = 109 \pm 3°$. The scale bars represent 0.5 mm.

S4.4. Experimental setup

The sketch of the experimental setup is given in Supporting Information Fig. S13. The condensation process is observed by using a microscope (BX51, Olympus, Japan) equipped with a CCD camera (UI-2220SE-M-GL, IDS, Germany). The samples are placed at ambient temperature of 21 ± 2 °C and humidity of $50 \pm 10\%$. The temperature of the cooling stage is kept at 2 ± 0.3°C.

As shown in Fig. S13, we give the schematic of the experimental setup. The key parts of the experimental setup consist of a microscope stage, a cooling stage, a refrigerator, an optical microscope (BX 51, Olympus, Japan) and a CCD camera (UI-2220SE-M-GL, IDS, Germany).

The cooling stage is fixed on the workbench of the microscope. The CCD camera is mounted on the eyepiece interface of the microscope. The refrigerator is connected to the cooling stage to guarantee that the temperature of the cooling state satisfies the required value for condensation. The samples are placed horizontally on the cooling stage. The top-view images are captured with the CCD camera during the condensation. The key parts of the components are put into a chamber (i.e., enclosed by the red dotted line in Fig. S13). In addition, a humidifier is placed in the chamber to maintain a moist ambient environment.
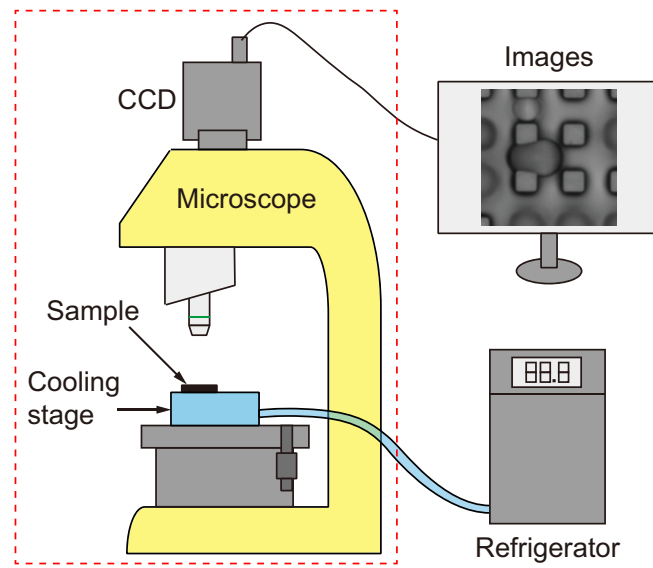

Fig. S13. Schematic showing the key parts of the experimental setup for the droplet condensation experiment.

S4.5. Experimental results

As shown in Fig. S14, condensation happens on the Glaco-coated substrate with $\theta_r = 156 \pm 3°$ and $H/L = 2$ (sample No. 4 in Table S1), and here we focus on one droplet. As the condensation progresses ($t < 79$ s), the diameter of droplet increases gradually. However, at $t = 80$ s, the diameter of droplet suddenly increases which means the spontaneous dewetting transition occurs, and the droplet jumps out of the pillars and locates at the top of the pillars. In addition, this wetting state transition could also be perceived by the sudden change of the grey levels of the two successive images (i.e., $t = 79$s and $t = 80$s). After the transition, the droplet continues to grow and its diameter increases smoothly (80 s $< t <$ 119 s). When the droplet grows big

enough ($t = 120$ s), it merges with the surrounding droplets and jumps out of the field of view.
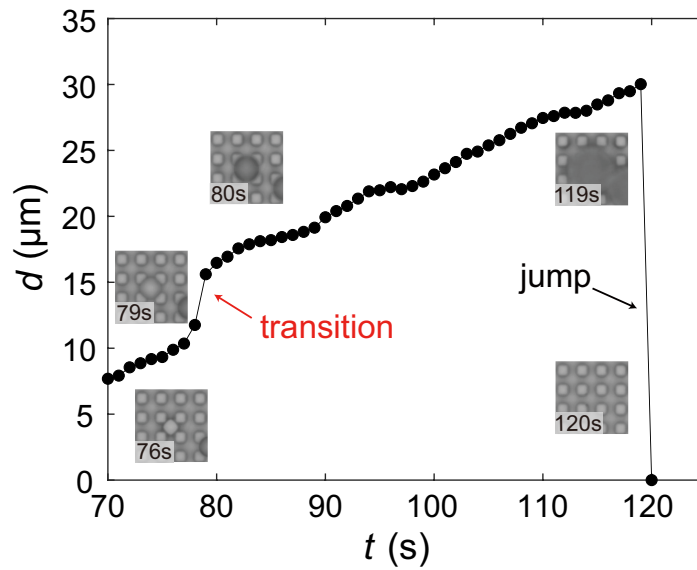

Fig. S14. Evolution of the droplet width with time. The insets along the experimental data correspond to $t =$ 76, 79, 80, 119 and 120 s, respectively. There is a dewetting at $t = 79$ s and a jumping at $t = 119$ s.

In order to verify the repeatability of our experimental results, we perform a large number of condensation experiments. Our experimental data are repeatable and we observed no less than 100 times repeatable condensation phenomena for each type of the wetting state transition. As examples shown in Fig. S15, we respectively show five times of the spontaneous dewetting mode (Fig. S15(a)), passive dewetting mode (Fig. S15(b)) and Wenzel wetting mode (Fig. S15(c)).
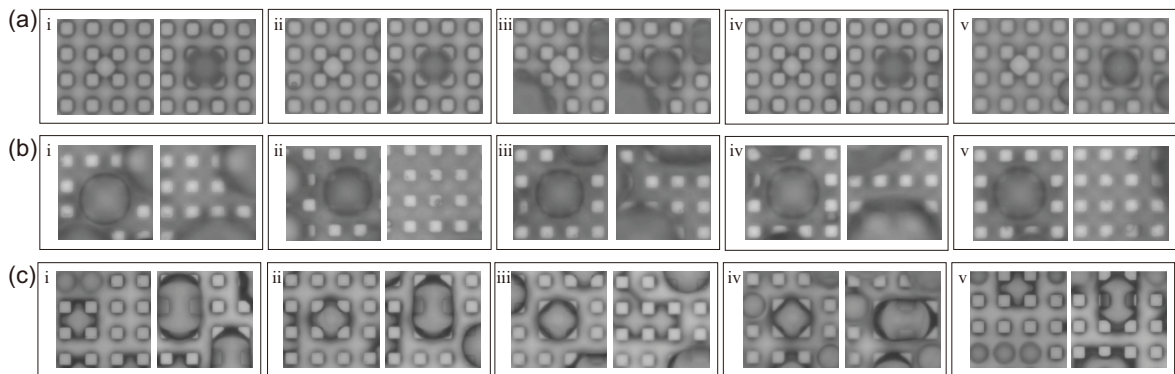

Fig. S15. Repeatability of the experimental results. Five examples of each wetting mode are given. (a) Spontaneous dewetting mode ($\theta_r = 156 \pm 3°$, $H/L = 2$, sample No. 2 in Table S1); (b) Passive dewetting mode

($\theta_r = 118 \pm 3°$, $H/L = 3$, sample No. 1 in Table S1); (c) Wenzel wetting mode ($\theta_r = 97 \pm 3°$, $H/L = 1.33$, sample No. 5 in Table S1).

In the above, we carry out LBM simulations using $S/L = 1.5$. Since the parameters of the micropillars in the experiment are fixed at $S/L = 1$ (see Table S1), as shown in Fig. S16, we supplement the LBM simulations (dots) by employing $S/L = 1$. The red and the black curves are the theoretical results that distinguish the Cassie-jumping, the Cassie-detaching and the Wenzel modes. It can be seen that when we change the value of S/L, the theoretical and simulation results (dots) remain consistent with each other very well. This indicates that the simulated results are generic to structures with different values of S/L.
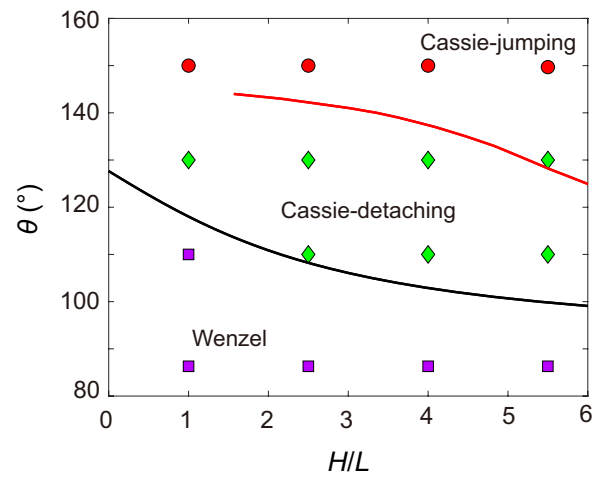

Fig. S16. Phase diagram of wetting state transitions of the condensed droplet with $S/L = 1$. The red, green and purple dots represent the simulation results of the Cassie-jumping, Cassie-detaching and Wenzel modes, respectively. The red and black curves are theoretical results of the boundaries.

Video legend

Video S1. Wetting state transition modes of the droplets by employing LBM simulations. The movie shows the entire processes of the wetting state transitions of the four modes. The upper left and right panels are the Cassie-jumping mode ($\theta = 150°$, $H/L = 2.5$) and Cassie-detaching mode ($\theta = 130$, $H/L = 2.5$), respectively. The bottom left and right panels are the Wenzel-collapsing ($\theta = 100°$, $H/L = 2.5$) and Wenzel-spreading mode ($\theta = 90°$, $H/L = 5.5$), respectively.

Video S2. Spontaneous dewetting of the droplet observed in the experiment. The geometrical parameters of the pillars are $L = 4$ μm, $S = 4$ μm and $H = 8$ μm, and the substrate is coated with Glaco. When condensation happens, a droplet appears and is confined in the four surrounding pillars. At $t = 80$ s, both the shape of the droplet and the gray levels of the two successive images suddenly change, suggesting an occurrence of dewetting, and the droplet escapes from the pillars but does not jump away from the substrate. The droplet continues to grow and finally merges with the surrounding droplets at $t = 120$ s and then disappears from the field of view.

Video S3. Passive dewetting of the droplet observed in the experiment. The geometrical parameters of the pillars are $L = 4$ μm, $S = 4$ μm and $H = 8$ μm, and the substrate is coated with fluoroacrylate. When condensation happens, a droplet appears and is confined in the four surrounding pillars. At $t = 184$ s, passive dewetting of the droplet happens when it merges with the surrounding droplets, and the droplet jumps out of the pillars.

Video S4. Wenzel wetting state transition observed in the experiment. The geometrical parameters of the pillars are $L = 6$ μm, $S = 6$ μm and $H = 8$ μm, and the substrate is coated with FDTS. When condensation happens, a droplet appears and is confined in the four surrounding pillars. As time progresses, the droplet gradually swallows the surrounding pillars and finally evolves to a wetting state at $t = 215$ s.

Reference

1. S. Chen and G. D. Doolen, Lattice Boltzmann method for fluid flows, *Annu. Rev. Fluid Mech.*, 1998, **30**, 329-364.
2. N. S. Martys and H. Chen, Simulation of multicomponent fluids in complex three-dimensional geometries by the lattice Boltzmann method, *Phys. Rev. E*, 1996, **53**, 743-750.
3. A. S. Joshi and Y. Sun, Multiphase lattice Boltzmann method for particle suspensions, *Phys. Rev. E*, 2009, **79**, 066703.
4. Y. Yu and Y. Liu, Lattice-Boltzmann models simulation of wetting modes on the surface with nanostructures, *J. Comput. Theor. Nanos.*, 2008, **5**, 1377-1380.

5. K. A. Raman, R. K. Jaiman, T.-S. Lee and H.-T. Low, Lattice Boltzmann simulations of droplet impact onto surfaces with varying wettabilities, *Int. J. Heat Mass Transf.*, 2016, **95**, 336-354.

6. R. Illner, *Lattice Boltzmann Modeling: An Introduction for Geoscientists and Engineers*. JSTOR, 2007.

7. X. Shan and H. Chen, Lattice Boltzmann model for simulating flows with multiple phases and components, *Phys. Rev. E*, 1993, **47**, 1815-1819.

8. K. A. Brakke, The surface evolver, *Exp. Math.*, 1992, **1**, 141-165.

9. I. Devic, J. M. E. Escobar and D. Lohse, Equilibrium drop shapes on a tilted substrate with a chemical step, *Langmuir*, 2019, **35**, 3880-3886.

10. T. H. Chou, S. J. Hong, Y. E. Liang, H. K. Tsao and Y. J. Sheng, Equilibrium phase diagram of drop-on-fiber: Coexistent states and gravity effect, *Langmuir*, 2011, **27**, 3685-3692.

11. D. J. Struik, *Lectures on Classical Differential Geometry*. Courier Corporation, 1961.

12. P.-G. de Gennes, F. Brochard-Wyart and D. Quéré, *Capillarity and Wetting Phenomena: Drops, Bubbles, Pearls, Waves*. Springer Science & Business Media, 2013.

13. C. Lv, P. Hao, X. Zhang and F. He, Dewetting transitions of dropwise condensation on nanotexture-enhanced superhydrophobic surfaces, *ACS Nano*, 2015, **9**, 12311-12319.

14. R. Dangla, S. Lee and C. N. Baroud, Trapping microfluidic drops in wells of surface energy, *Phys. Rev. Lett.*, 2011, **107**, 124501.

15. R. Dangla, S. C. Kayi and C. N. Baroud, Droplet microfluidics driven by gradients of confinement, *Proc. Natl. Acad. Sci. U.S.A.*, 2013, **110**, 853-858.

16. C. W. Park and G. M. Homsy, Two-phase displacement in Hele Shaw cells: Theory, *J. Fluid Mech.*, 2006, **139**, 291-308.

17. I. U., Vakarelski, N. A. Patankar, J. O. Marston, D. Y. Chan and S. Thoroddsen, Stabilization of Leidenfrost vapour layer by textured superhydrophobic surfaces, *Nature*, 2012, **489**, 274-277.

18. G. Dupeux, P. Bourrianne, Q. Magdelaine, C. Clanet and D. Quéré, Propulsion on a superhydrophobic ratchet, *Sci. Rep.*, 2014, **4**, 5280.